PAPER • OPEN ACCESS

Modeling of high power impulse magnetron sputtering discharges with tungsten target

To cite this article: Swetha Suresh Babu *et al* 2022 *Plasma Sources Sci. Technol.* **31** 065009

View the article online for updates and enhancements.

Modeling of high power impulse magnetron sputtering discharges with tungsten target

Swetha Suresh Babu[1], **Martin Rudolph**[2], **Daniel Lundin**[3],
Tetsuhide Shimizu[4], **Joel Fischer**[3], **Michael A Raadu**[5],
Nils Brenning[3,5] **and Jon Tomas Gudmundsson**[1,5,*]

[1] Science Institute, University of Iceland, Dunhaga 3, IS-107 Reykjavik, Iceland
[2] Leibniz Institute of Surface Engineering (IOM), Permoserstraße 15, 04318 Leipzig, Germany
[3] Plasma and Coatings Physics Division, IFM-Materials Physics, Linköping University, SE-581 83 Linköping, Sweden
[4] Department of Mechanical Systems Engineering, Graduate School of Systems Design, Tokyo Metropolitan University, 6-6, Asahigaoka, Hino-shi, 191-0065 Tokyo, Japan
[5] Space and Plasma Physics, School of Electrical Engineering and Computer Science, KTH Royal Institute of Technology, SE-10044 Stockholm, Sweden

E-mail: tumi@hi.is

CrossMark

Abstract

The ionization region model (IRM) is applied to model a high power impulse magnetron sputtering discharge with a tungsten target. The IRM gives the temporal variation of the various species and the average electron energy, as well as internal discharge parameters such as the ionization probability and the back-attraction probability of the sputtered species. It is shown that an initial peak in the discharge current is due to argon ions bombarding the cathode target. After the initial peak, the W^+ ions become the dominating ions and remain as such to the end of the pulse. We demonstrate how the contribution of the W^+ ions to the total discharge current at the target surface increases with increased discharge voltage for peak discharge current densities $J_{D,peak}$ in the range 0.33–0.73 A cm^{-2}. For the sputtered tungsten the ionization probability increases, while the back-attraction probability decreases with increasing discharge voltage. Furthermore, we discuss the findings in terms of the generalized recycling model and compare to experimentally determined deposition rates and find good agreement.

(Some figures may appear in colour only in the online journal)

1. Introduction

The magnetron sputtering discharge is a highly successful and widely used thin film deposition technique [1, 2] that falls into the category of physical vapor deposition processes. In the magnetron sputtering discharge a dense plasma is maintained in the cathode vicinity by a static magnetic field that traps the electrons. This is achieved by maintaining a relatively weak magnetic field (typically $B(z, r) < 100$ mTesla), and therefore electrons are the only magnetized species within the discharge [3]. In the dc magnetron sputtering (dcMS) discharge the film-forming material is mainly composed of neutral atoms, the ionization of the sputtered film-forming species is small, and the ions available in the discharge are ions of the noble working gas [4]. Often, it is desired to have a high degree of ionization in the flux of the film-forming material, as it gives overall improved thin film quality [5, 6]. This can be achieved by applying high power pulses at low repetition

frequency and low duty cycle to the cathode target. This approach is referred to as high power impulse magnetron sputtering (HiPIMS) [2, 4, 5].

Tungsten (W) is a refractory metal with a range of diverse applications. It has the highest melting temperature ($T_m = 3695$ K) and the lowest thermal expansion coefficient (4.5×10^{-6} K^{-1}) among the elemental metals and has a low electrical resistivity. Therefore, tungsten is used for metallization in microelectronics, including as interconnects and contact plugs, and as a diffusion barrier [7, 8]. Currently, tungsten is considered as the most promising candidate as the divertor target material in thermonuclear fusion reactors due to its high threshold energy for sputtering by hydrogen and helium ions, high melting point, large thermal shock resistance, good handling with respect to machining, and low vapor pressure [9, 10]. Tungsten oxide (WO$_3$) thin films are of interest as electrochromic materials due to their chemical stability, strong adherence to a number of substrates, and high coloration efficiency [11]. Tungsten oxide films also have applications as the active layer in hydrogen gas sensors [12].

Deposition of tungsten thin films by dcMS and HiPIMS results in textured films that consists of two phases, the equilibrium α–W (A2 bcc) and the metastable β–W (A15 cubic). The HiPIMS-deposited films are denser, have smaller grains and better adhesion [13–15]. Furthermore, HiPIMS-deposited tungsten thin films exhibit enhanced properties, including smoother surfaces, higher hardness, and Young's modulus values [13, 16, 17]. In some of these studies an external magnetic field was added, by placing a toroidal-shaped permanent magnet in front of the cathode target [16, 17]. Recently, Shimizu *et al* [15] demonstrated stress-free, unstrained single phase α–W thin films, deposited without post-annealing, through synchronized pulsed substrate bias that selectively enhances the energy of the metal population of the ion bombardment. They also reported on the temporal behavior of ion and neutral species of the discharge determined by time-resolved optical emission spectrometry (OES). The OES measurements show that the emission from excited neutral argon increases rapidly at the beginning of the pulse and peaks at 4 μs into the 100 μs long pulse. The emission from the Ar$^+$ ions peaks a few microseconds into the pulse and then decays. This is followed by an increase in emission from atomic W and W$^+$ ions which indicates ejection of tungsten atoms from the target and subsequent ionization. The emission from the W$^+$ ions peaks at roughly 35 μs into the pulse and then it stabilizes at a level that remains constant until the end of the pulse.

The ionization region model (IRM) is a time-dependent volume-averaged plasma chemical model of the ionization region (IR), located in the close vicinity of the target racetrack, defined by the confining magnetic field. It was developed to study the discharge behavior during a HiPIMS pulse and the afterglow [18–20]. The IRM has been applied to study various processes, such as gas rarefaction and refill processes [18], and the electron heating mechanisms [21], in an argon HiPIMS discharge with an Al target, and the feasibility of ionizing carbon in a discharge with a graphite target [22]. Earlier we have demonstrated that in HiPIMS discharge operation a significant fraction of the discharge current is due to

recycling, either working gas recycling or self-sputter (SS) recycling [23]. In what was coined as the generalized recycling model, a primary current acts as a seed that is amplified by the SS process and the working gas-recycling process. For a HiPIMS discharge with an aluminum [19, 23, 24] and a copper [25] target, the discharge reaches almost a complete SS recycle operation when operated in the HiPIMS regime, while a discharge with a graphite target [22] and reactive sputtering with a poisoned target [26, 27] operates in working gas recycling mode. However, so far the understanding of the plasma processes in a HiPIMS discharge with a tungsten target is limited. Here, we explore a HiPIMS discharge with a tungsten target using the IRM. Tungsten (7.98 V) has a higher ionization potential than Cu (7.73 V), Ti (6.83 V), and Al (5.99 V), and is therefore more difficult to ionize, while it has a sputter yield slightly higher than titanium, and has a higher atomic mass. Earlier, a volume-averaged model has been developed to describe a reactive HiPIMS discharge and to model the deposition of WO$_3$ films from a tungsten target in Ar/O$_2$ mixture [28]. The model results indicate that the degree of tungsten ionization increases from 50% to 80% as the power density is increased from 100–500 W cm^{-2}, and it also increases with increased pulse length. Furthermore, it is claimed that W$^+$ ions are re-implanted into the target which effectively decreases the target oxide coverage during reactive sputtering [28].

Here we extend the IRM to include a reaction set for a tungsten discharge. We apply the model to study a HiPIMS discharge formed with argon as the working gas and a tungsten cathode target in the discharge setup that was earlier explored experimentally by Shimizu *et al* [15] and used to deposit thin tungsten films. The IRM is described in section 2, where the reaction set for tungsten is also discussed. The experimental discharges that are to be analyzed are discussed in section 3. In section 4, the IRM is applied to discharges with a tungsten target to determine the temporal evolution of the particle densities, the ionization and back-attraction probabilities of the tungsten species, the working gas rarefaction, and the ionized flux fraction, as the discharge voltage is varied. In section 5, the findings are discussed in terms of the generalized recycling model. The results are summarized in section 6.

2. The ionization region model

The IRM is a plasma chemistry model that assumes volume-averaged values over the entire IR volume for the electron, ion and neutral densities and the electron temperature. Using the IRM, the time evolution of neutral and charged species and the electron temperature in pulsed magnetron sputtering discharges can be evaluated and explored further. This includes the temporal development of the electron energy and the particle densities for all the heavy particles, which are defined by a set of ordinary differential equations [19]. The IRM provides information on internal discharge properties including the ionization probability, the back-attraction probability, the voltage drop across the IR, and the electrical power transfer to the electrons. The model is limited to the IR, which is defined as an

annular cylinder with outer radius r_{c2}, and inner radius r_{c1} sitting above the racetrack, and a length $L = z_2 - z_1$, extending from z_1 to z_2 axially away from the target. Geometrical effects are included indirectly as loss and gain rates across the boundaries of this annular cylinder to the target and the bulk plasma (the diffusion region (DR)) [18]. The IRM allows us to determine the flux and ionization fraction as target species in the material flux from the IR to the DR that is deposited onto the substrate (located in the DR). The electron density is found by applying the quasi-neutrality condition.

The plasma-chemical reactions are described by two sets of rate coefficients, one for the cold and the other set for the hot electron population. The cold electrons are created by ionization of argon and tungsten atoms, while the hot electrons are ion-induced secondary electrons, emitted from the target surface, and consequently accelerated across the cathode sheath [29]. The majority of the electrons belong to the cold Maxwellian electron population, which therefore dictates the electron density and the effective electron temperature. The rate coefficients are calculated assuming a Maxwellian electron energy distribution function (EEDF) and fit in the range $T_e = 1$–7 eV for cold electrons, and in the range 200–1000 eV for hot electrons. A good agreement has been demonstrated between the bi-Maxwellian electron energy distribution assumed by the IRM and the electron energy distribution calculated by the Orsay Boltzmann equation for electrons coupled with ionization and excited states kinetics (OBELIX) model, a collisional-radiative model coupled with a Boltzmann solver [29]. The reaction set and the rate coefficients involving argon in the IRM are mostly the same as used in our earlier work on HiPIMS discharges with titanium target [26, 30, 31] with a few modifications of the rate coefficients involving the metastable argon atom [29], the consideration of the afterglow [20], and addition of Ar^{2+} ions [22]. Note that the argon atoms in the ground state are assumed to be split into three groups depending on their kinetic energy: cold argon atoms Ar^C are the atoms in the ground state in the feedstock gas at the gas temperature, hot argon Ar^H are atoms in the ground state which return from the target immediately after the argon ion impact event, with a typical sputter energy of a few eV, and warm argon Ar^W are atoms in the ground state that were implanted in the target at the location of ion impact, and return to the surface and leave with the target temperature, at most 0.1 eV [19, 24]. A detailed description of the IRM, including a discussion of the various generation and loss terms for each of the species, is given by Huo *et al* [19].

2.1. Reactions involving tungsten

The tungsten atoms enter the discharge as they are sputtered off the cathode target due to ion bombardment. The rate at which tungsten atoms are sputtered off the target is given by a generation term [19]

$$R_{W,sputt} = \frac{\sum_i \Gamma_i^{RT} S_{RT} Y_i(\mathcal{E}_i)}{\mathcal{V}_{IR}} \quad (m^{-3} \ s^{-1}), \tag{1}$$

where i stands for the ion involved in the process, here $i = W^+$, W^{2+}, Ar^+, or Ar^{2+}, and Γ_i^{RT} is the flux of ion

i towards the target in $(m^{-2} \ s^{-1})$, S_{RT} is the area of the sputtered region (racetrack), $Y_i(\mathcal{E}_i)$ is the energy-dependent sputter yield for ion i bombarding the target, and $\mathcal{V}_{IR}$ is the total volume of the IR. The sputter yield for each ion i is given by a fit following the general form

$$Y_i = a\mathcal{E}_i^b, \tag{2}$$

where $\mathcal{E}_i$ is the energy of the incoming ion and a and b are constants that depend on the ion target pair. For argon ions bombarding tungsten $a = 0.0429$ and $b = 0.521$, and for SS of tungsten $a = 0.0066$ and $b = 0.770$ [42] derived from fits to the sputter yields calculated using the TRansport of Ions in Matter code [43]. These parameters are valid in the ion energy range typical for magnetron sputtering or up to 2000 eV.

The atoms sputtered off the target are injected into the IR with a velocity corresponding to $1/2 \times \mathcal{E}_{cohesive} = 1/2 \times 8.9$ eV $= 4.45$ eV [44, p 50], where $\mathcal{E}_{cohesive}$ is the cohesive energy of the target material. These atoms participate in the discharge and are subject to collisions with other plasma species. This includes electron impact ionization and excitation of the tungsten atom. The ground state of the tungsten atom is denoted $[Xe]4f^{14}5d^46s^2 \ ^5D_0$. The cross section for electron impact ionization of the tungsten atom is taken from the calculation by Deutsch *et al* [39] with an ionization potential of 7.864 eV. The cross section for electron impact ionization of singly charged tungsten ions is taken from the measurements by Montague and Harrison [40]. The rate coefficient for the charge transfer $Ar^+ + W$ is based on the value estimated for the same reaction with Cu [41]. For Penning ionization of tungsten through collisions with metastable argon atoms we use published cross sections [45–47] which were scaled by the square of the atomic radius, atom mass, and the number of valence electrons [48] and assume the sputtered species to have an average energy of 3 eV. All the reactions and rate coefficients included in the IRM for this current study are listed in table 1. To calculate the collisional energy loss per electron–tungsten ion pair created $\mathcal{E}_c$, we use the electron impact ionization cross section from Deutsch *et al* [39]. Furthermore, we include the lowest excited levels of tungsten listed in table 2 and assume that each excitation cross section follows the Thomson cross section [49, p 70–72] with a peak at 1/10 of the peak of the ionization cross section. Note that these excited states of the tungsten atom are only included here to account for energy loss but are not treated as species. The cross section for electron elastic scattering with a tungsten atom is taken from the work of Blanco *et al* [50]. These cross sections are used to calculate the energy loss per electron–ion pair created for tungsten that is shown in figure 1. The figure also shows the energy loss per electron–ion pair created for ground state argon atom calculated as discussed elsewhere [26]. As expected the energy loss per electron–ion pair created for tungsten is lower than for argon.

For the secondary electron emission yield due to bombardment by argon ions we use the value of 0.094, which is taken from the measurements of Hagstrum [51], determined by averaging over all the values measured for ion bombarding energy in the range up to 1000 eV. In this ion energy

Table 1. The reactions and rate coefficients used in the IRM for a discharge with argon as the working gas and tungsten cathode target including both hot and cold electrons. The rate coefficients are calculated assuming a Maxwellian EEDF and fit in the range $T_e = 1$–7 eV for cold electrons and 200–1000 eV for hot electrons. The rate coefficients in the reaction set for argon are taken from earlier works [22, 29].

	Reaction	Threshold (eV)	Rate coefficient (m³ s⁻¹)	Electrons	References
(R1)	$e + Ar(3p^6) \rightarrow Ar^+ + e + e$	15.76	$2.34 \times 10^{-14} T_e^{0.59}\, e^{-17.44/T_e}$	Cold	[32]
			$8 \times 10^{-14} T_e^{0.16}\, e^{-27.53/T_e}$	Hot	
(R2)	$e + Ar(3p^6) \rightarrow Ar(4s[3/2]_2) + e$	11.548	$1.617 \times 10^{-14} T_e^{-0.8238} \exp(-14.1256/T_e)$	Cold	[33, 34]
			$1.1397 \times 10^{-22} T_e^2 - 1.8975 \times 10^{-19} T_e + 8.7910 \times 10^{-17}$	Hot	
(R3)	$e + Ar(3p^6) \rightarrow Ar(4s'[1/2]_0) + e$	11.723	$2.86 \times 10^{-15} T_e^{-0.8572} \exp(-14.6219/T_e)$	Cold	[33, 34]
			$1.8045 \times 10^{-23} T_e^2 - 2.9825 \times 10^{-20} T_e + 1.357 \times 10^{-17}$	Hot	
(R4)	$e + Ar(4s[3/2]_2) \rightarrow Ar(3p^6) + e$		$3.23 \times 10^{-15} T_e^{-0.8238} \exp(-2.578/T_e)$	Cold	Detailed
			$(1.1397 \times 10^{-22} T_e^2 - 1.8975 \times 10^{-19} T_e + 8.7910 \times 10^{-17})/5$	Hot	Balancing
(R5)	$e + Ar(4s'[1/2]_0) \rightarrow Ar(3p^6) + e$		$2.86 \times 10^{-15} T_e^{-0.8572} \exp(-2.8989/T_e)$	Cold	Detailed
			$1.8045 \times 10^{-23} T_e^2 - 2.9825 \times 10^{-20} T_e + 1.357 \times 10^{-17}$	Hot	Balancing
(R6)	$e + Ar(4s'[1/2]_0) \rightarrow Ar^+ + 2e$	4.21	$1.143\,56 \times 10^{-13} T_e^{0.2548} \exp(-4.4005/T_e)$	Cold	[35, 36]
			$1.5213 \times 10^{-19} T_e^2 - 2.9599 \times 10^{-16} T_e + 1.8155 \times 10^{-13}$	Hot	
(R7)	$e + Ar(4s[3/2]_2) \rightarrow Ar^+ + 2e$	4.21	$1.143\,56 \times 10^{-13} T_e^{0.2548} \exp(-4.4005/T_e)$	Cold	[35, 36]
			$1.5213 \times 10^{-19} T_e^2 - 2.9599 \times 10^{-16} T_e + 1.8155 \times 10^{-13}$	Hot	
(R8)	$e + Ar^+ \rightarrow Ar^{2+} + 2e$	27.63	$8.6365 \times 10^{-15} T_e^{0.6746} \exp(-24.3019/T_e)$	Cold	[37]
			$5.22 \times 10^{-14} - 4.943 \times 10^{-17} T_e$	Hot	[a]
(R9)	$e + Ar \rightarrow Ar^{2+} + 3e$		—	Cold	[38]
			$6.169 \times 10^{-15} - 1.6316 \times 10^{-17} T_e$	Hot	[b]
(R10)	$e + W \rightarrow W^+ + e$	7.864	$6.3966 \times 10^{-14} T_e^{0.4839} \exp(-8.221/T_e)$	Cold	[39]
			$4.2507 \times 10^{-10} T_e^{-1.1791} \exp(-256.38/T_e)$	Hot	
(R11)	$e + W^+ \rightarrow W^{2+} + e$	16.35	$1.446 \times 10^{-14} T_e^{0.7143} \exp(-14.5193/T_e)$	Cold	[40]
			$4.673 \times 10^{-10} T_e^{-1.3047} \exp(-273.55/T_e)$	Hot	
(R12)	$Ar^+ + W \rightarrow Ar + W^+$		2×10^{-16}		[41]
(R13)	$Ar(4s'[1/2]_0) + W \rightarrow Ar + W^+ + e$		5.3×10^{-15}		See text
(R14)	$Ar(4s[3/2]_2) + W \rightarrow Ar + W^+ + e$		5.3×10^{-15}		See text

[a] This is a fit for T_e in the range 200–700 eV.
[b] This is a fit for T_e in the range 100–200 eV.

Table 2. The reactions, threshold energies and references to cross sections used to calculate the collisional energy loss for tungsten.

	Reaction	$\mathcal{E}_{th}$ (eV)	Reference
(R15)	$e + W \to W^+ + e$	7.864	[39]
(R16)	$e + W \to W + e$	$3(m_e/M_W)T_e$	[50]
(R17)	$e + W(^5D_0) \to W(^5D_1) + e$	0.207	
(R18)	$e + W(^5D_0) \to W(^5D_2) + e$	0.412	
(R19)	$e + W(^5D_0) \to W(^5D_3) + e$	0.598	
(R20)	$e + W(^5D_0) \to W(^5D_4) + e$	0.771	
(R21)	$e + W(^5D_0) \to W(^7S) + e$	0.366	
(R22)	$e + W(^5D_0) \to W(^3P_{2_0}) + e$	1.181	
(R23)	$e + W(^5D_0) \to W(^3P_{2_1}) + e$	1.650	
(R24)	$e + W(^5D_0) \to W(^3P_{2_2}) + e$	2.387	
(R25)	$e + W(^5D_0) \to W(^3H_4) + e$	1.508	
(R26)	$e + W(^5D_0) \to W(^3H_5) + e$	1.868	
(R27)	$e + W(^5D_0) \to W(^3H_6) + e$	2.109	
(R28)	$e + W(^5D_0) \to W(^3G) + e$	1.655	
(R29)	$e + W(^5D_0) \to W(^3F2) + e$	1.708	
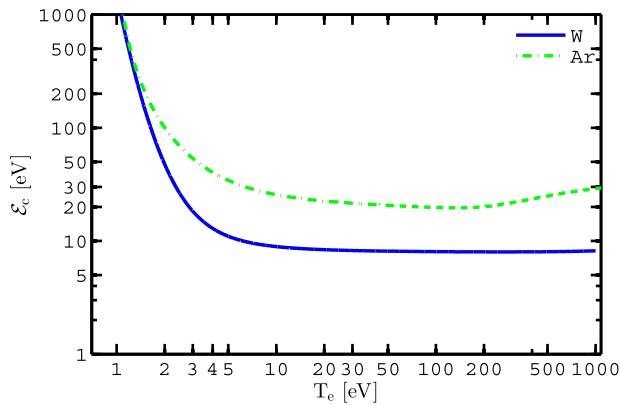
Figure 1. The collisional energy loss per electron–ion pair created, $\mathcal{E}_c$, as a function of the electron temperature for the ground state tungsten and argon atoms, calculated assuming a Maxwellian electron energy distribution.

range the electron emission is due to potential emission which appears to give roughly constant electron emission yield. For the tungsten ions bombarding the tungsten target the secondary electron emission yield is essentially zero. We neglect secondary electron emission due to bombardment of the target by W^{2+} ions.

3. Experimental apparatus and method

The IRM is a semi-empirical discharge model of a physical HiPIMS discharge and therefore requires input from an experiment. These inputs include the working gas pressure, the target material, discharge current and voltage waveforms, the dimensions of the target, and the dimensions of the IR. Here, the discharge voltage and current waveforms measured for a HiPIMS discharge in argon with a tungsten target are analyzed using the IRM. The discharge parameters were measured for a discharge with a planar circular unbalanced magnetron assembly with a tungsten (99.999% in purity) disk of diameter 75 mm, and a thickness of 5 mm, as the cathode target, and with argon working gas of purity of 99.997% at a constant flow rate of
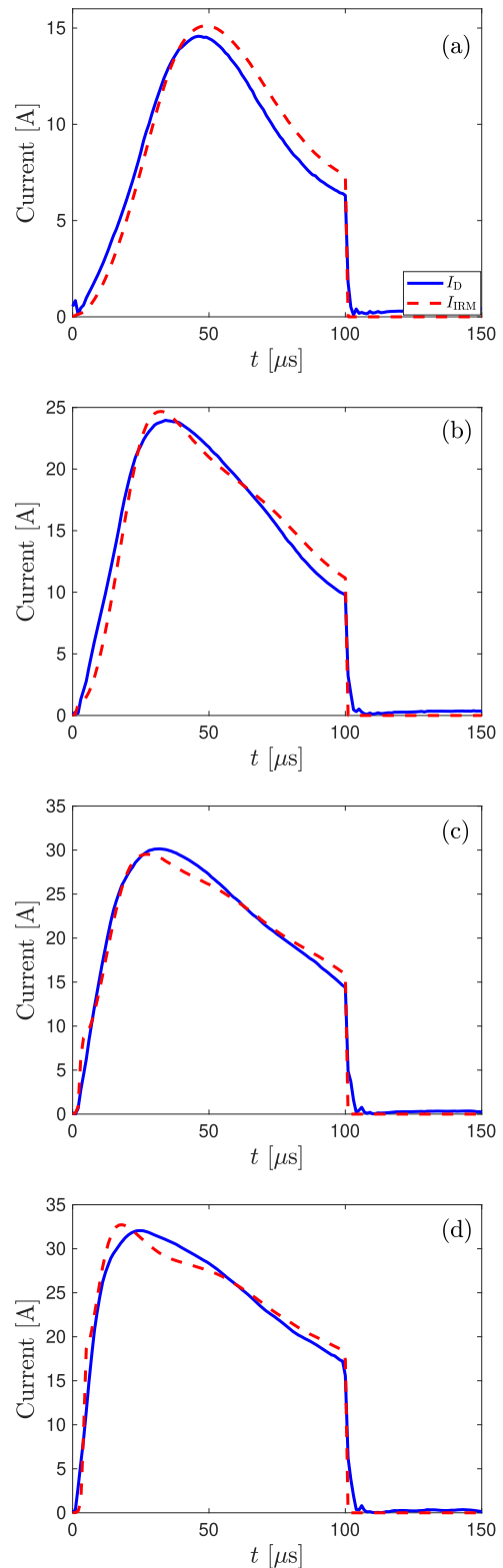
Figure 2. The measured temporal evolution of the discharge current (solid line) and the model fit (dashed line) for discharge voltages of (a) 500 V, (b) 600 V, (c) 700 V, and (d) 800 V, for a discharge with 75 mm diameter tungsten target.

100 sccm which was maintained at a constant working gas pressure of 1.0 Pa by adjusting the pumping speed via the main gate valve. Unipolar HiPIMS pulses, 100 μs in length, were supplied by a HiPSTER 1 pulsing unit fed by a 1 kW

HiPSTER 1-DCPSU DC power supply (Ionautics AB, Sweden) [15]. The details of the experimental setup and some measured discharge properties as well as the resulting thin tungsten films are discussed by Shimizu *et al* [15]. Based on the earlier work [15] the discharge current waveforms were measured for this current work for four different discharge voltages 500 V, 600 V, 700 V, and 800 V. There are slight differences in the discharge current characteristics compared to the earlier report as the target is somewhat more eroded. The measured discharge current waveforms for the various applied discharge voltages are shown in figure 2. The average power is maintained to be roughly the same for all cases by varying the repetition frequency. For each discharge voltage and current waveform pair in HiPIMS operation the deposition rate was determined. Furthermore, the deposition rate for a dcMS discharge operated at the same average power was determined. We assume the deposition rate from the dcMS operation to be proportional the total flux (atoms s^{-1}) of atoms sputtered from the target Γ_0, and the deposition rate in HiPIMS operation is assumed to be proportional to the flux of sputtered species (ions and neutrals) that leave the IR towards the DR Γ_{DR}. In this way the normalized deposition rate $F_{dep} = \Gamma_{DR}/\Gamma_0$ can be determined for each set of discharge voltage and discharge current waveforms.

4. Model results

The IRM is used to determine the temporal variation of the species densities along with a few internal discharge parameters for four different discharge voltages that exhibit the discharge current waveforms shown in figure 2. The volume parameters of the IR were set as follows: $r_{c1} = 8$ mm, $r_{c2} = 27$ mm, $z_1 = 2$ mm, and $z_2 = 22$ mm. Using the IRM, a best fit is determined where the experimentally determined discharge current waveform for each of the discharge voltages is best reproduced by the modeled discharge current. The IRM has three unknown fitting parameters: (i) the ion back-attraction probability for the metal ions $\beta_{t,pulse}$ and gas ions $\beta_{g,pulse}$ during the pulse on time (here we assume $\beta_{t,pulse} = \beta_{g,pulse}$ as in earlier studies [18, 19, 29, 52, 53]), (ii) the potential drop across the IR, V_{IR}, and (iii) the electron recapture probability r. The voltage drop across the IR is incorporated using the ratio $f = V_{IR}/V_D$ [19]. For a metal target the electron recapture probability r, can be varied in the range $0.25 \leqslant r \leqslant 0.9$ without influencing the model output much. For the cases presented here, the electron recapture probability r has been set to $r = 0.5$ [54]. This leaves the ($\beta_{t,pulse}$, f) parameter space to be explored through the model fitting procedure. The best fit is found using a fitting map showing the fraction of the discharge voltage that drops across the IR $f = V_{IR}/V_D$ versus the back-attraction probability of an ion of the sputtered species during the pulse $\beta_{t,pulse}$ [53], and is shown in figure 3. In this figure the root mean square deviation between the modelled and the experimental peak discharge current is color-coded such that the blue zones in the fitting map indicate the combinations of $f = V_{IR}/V_D$ and $\beta_{t,pulse}$ where the least square error is the smallest and the modeled discharge current resembles the experimental waveform the best. The dark blue
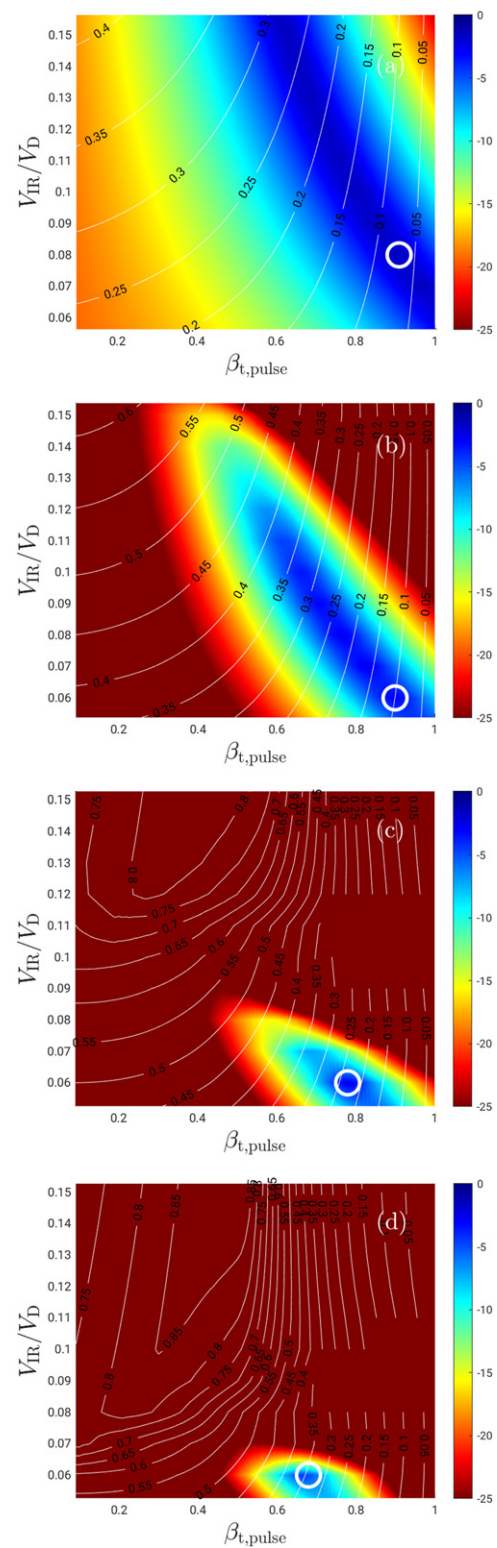
Figure 3. The fitting maps showing $f = V_{IR}/V_D$ versus the back attraction probability $\beta_{t,pulse}$ for discharge voltages of (a) 500 V, (b) 600 V, (c) 700 V, and (d) 800 V, for a discharge with 75 mm diameter tungsten target. The white circles indicate where a well fitted discharge current profile is observed. The white lines and the accompanying numbers indicate the ionized flux fraction.

zones remain somewhat in the same region (combinations of f and $\beta_{t,pulse}$) for the varying discharge voltages but the area of the blue region decreases with increased discharge voltage.

Table 3. Parameters derived from the modeling of a HiPIMS discharges with tungsten target.

V_D (V)	$I_{D,peak}$ (A)	$J_{D,peak}$ (A cm^{-2})	Rarefaction (%)	α_t	$\beta_{t,pulse}$	β_t	$f = V_{IR}/V_D$	F_{flux}
500	14.56	0.33	57.3	0.54	0.91	0.87	0.08	0.07
600	23.96	0.54	63.8	0.62	0.90	0.87	0.06	0.09
700	30.14	0.68	72.1	0.70	0.78	0.75	0.06	0.23
800	32.06	0.73	75.9	0.75	0.68	0.66	0.06	0.34

Note that a larger blue area is apparent for the discharge with a discharge voltage of 500 V, which indicates that there are significantly higher uncertainties in the determined values for this case. The resulting best fits determined by the IRM for each of the discharge current waveforms are also shown with dashed lines in figure 2. The fits are generally very good for most of the pulse-on time.

The sputtered species are assumed to initially have a directional velocity away from the target. Consequently, the ions of the sputtered species are assumed to have the same directional velocity. In HiPIMS operation a significant fraction of the deposition flux is made of ionized tungsten, which we will confirm later is indeed the case. The potential drop across the IR constitutes a potential barrier, which prevents some of the tungsten ions from reaching the substrate, and therefore they do not contribute to the deposition rate. This potential barrier is eliminated after the pulse-on time. Therefore, we assume β_t to be zero in the afterglow and consequently the back-attraction probability is defined as [20]

$$\beta_t(t) = \begin{cases} \beta_{t,pulse} & \text{during the pulse} \\ 0 & \text{in the afterglow.} \end{cases} \quad (3)$$

The flux toward the DR is calculated from the flux toward the racetrack during the pulse [19, 55]. After the pulse has been switched off, the ions are assumed to have a velocity that is similar to that of the sputtered metal species. The back-attraction probability during the pulse is found to be in the range $\beta_{t,pulse} \approx 0.68$–0.91, decreasing with increasing peak discharge voltage. The overall back-attraction probability β_t is somewhat lower or in the range 66%–87%. The fraction of the discharge voltage that drops over the IR is rather low or in the range $f = V_{IR}/V_D = 6\%$–8%. Some of the key discharge parameters derived from the IRM, including the ionization probability, the back-attraction probability of the sputtered species, and the ionized flux fraction for the various discharge voltages are listed in table 3.

The temporal evolution of the neutral particle densities is shown in figure 4. Overall the temporal evolution of the neutral particle densities are similar for the various discharge voltages. The ground state working gas argon atoms dominate the discharge. The cold (or primary) argon ground state density (denoted $Ar^C(3p^6)$ in figure 4) decreases steadily to a minimum at the end of the pulse, which indicates working gas rarefaction [56]. Working gas rarefaction is known to occur and be rather significant in HiPIMS discharges as has been demonstrated experimentally [15, 57–59]. Actually, Shimizu *et al* [15] noted that the working gas rarefaction is particularly pronounced for the case of tungsten. Before the pulse initiation the density
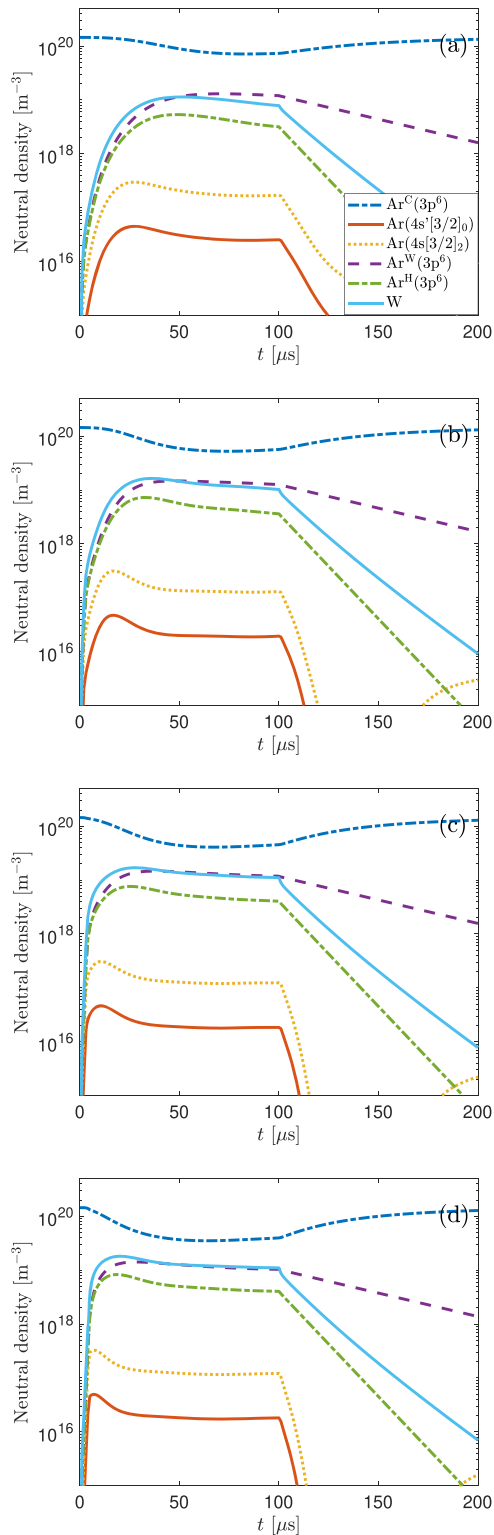
of cold ground state argon atoms at 1 Pa and $T_g = 500$ K is 1.4×10^{20} m^{-3}. Figure 4 shows that there is an increase in both the hot (Ar^H) and warm (Ar^W) argon atom densities to a peak, during the pulse, and then a slight decrease again. Note that the total argon ground state density is composed of the cold, warm and hot densities or $[Ar(3p^6)] = [Ar^C(3p^6)] + [Ar^W(3p^6)] + [Ar^H(3p^6)]$. The temporal evolution of the total argon density as a percentage of the density at the start of the pulse ($n_{Ar}/n_{Ar,0}$), is shown in figure 5 for all the discharge voltages explored. With increased discharge voltage, the degree of rarefaction $1 - (n_{Ar}/n_{Ar,0})$ increases from 57% at 500 V (0.33 A cm^{-2}) to 76% at 800 V (0.73 A cm^{-2}). Note that there are several factors that contribute to rarefaction, including electron impact ionization of argon atoms and kick-out of argon atoms by the sputter wind, which is then balanced by diffusional refill of cold argon from the bulk plasma, returning hot and warm argon atoms from the target, and charge exchange $Ar^+ + M \rightarrow Ar + M^+$ (very small contribution) [52].

We find that the kick-out of argon atoms by the sputter wind is the dominating process leading to working gas rarefaction for a HiPIMS discharge with a tungsten target for peak current densities $J_{D,peak}$ in the range 0.33–0.73 A cm^{-2}. For comparison, Huo *et al* [52] using the IRM observed a reduction by up to 50% for a 400 μs pulses with an aluminium target at 0.6 A cm^{-2} and the dominating contributor to the working gas rarefaction is electron impact ionization of argon atoms. For a discharge with graphite target Eliasson *et al* [22] estimated up to 66% rarefaction for 50 μs pulses and current density of 1 A cm^{-2}.

Figure 4 also shows that the tungsten atom density increases rapidly early in the pulse and remains stable throughout the pulse. After the end of the pulse when the sputtering by energetic ion bombardment comes to an end, the density of the ground state tungsten atoms decreases sharply at first and then more slowly.
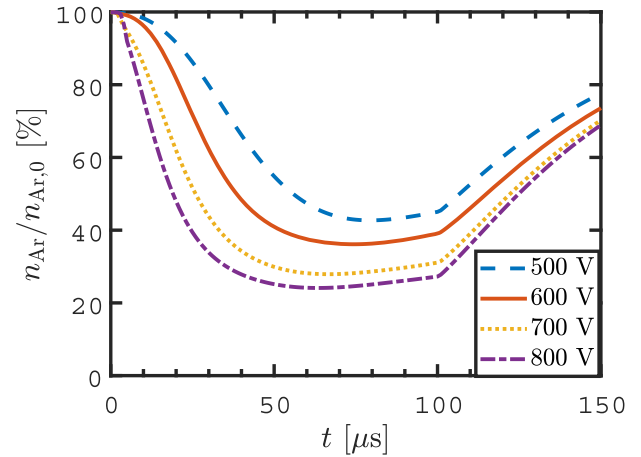
The temporal evolution of the charged particle densities are shown in figure 6. Initially, the Ar^+ ion is the dominating ion but soon the W^+ ion takes over and remains the dominating ion towards the end of the pulse. The density of the doubly charged W^{2+} ions is always smaller than the density of the Ar^+ ions and the density of the Ar^{2+} ions significantly smaller. For comparison the total neutral argon density $[Ar^0]$ and the neutral tungsten density $[W^0]$ are shown as well in figure 6. Shimizu *et al* [15] applied time-resolved optical emission spectroscopy (OES) and mass spectrometry on a HiPIMS discharge with a tungsten target to monitor the time evolution of the plasma ion-composition reaching the substrate. The measurements show that the emission from excited neutral argon increases

Figure 5. The temporal evolution of the total argon neutral density (ground state and excited states) as a percentage of the density at the start of the pulse for the various discharge voltages with 75 mm diameter tungsten target.

at roughly 35 μs into the pulse and then it stabilizes at a level that remains constant until the end of the pulse. They found the ion-composition to be initially working gas-dominated, but observed a window ranging from 30 to 120 μs from the pulse initiation when metal ions are dominating, having more than 50% of the total ion intensity. This they claim to be both due to efficient ionization of sputtered species during the pulse and a strong working gas rarefaction. After the end of the pulse duration the ions of the working gas dominate again. The emission intensity from the W^{2+} ions was always more than an order of magnitude weaker than from the W^+ ions. Therefore, the model results shown in figure 6 agree with the experimental findings. It should be noted that the measured time-averaged ion energy distributions for the W^+ ions exhibit a high energy tail [16], which is commonly observed in HiPIMS discharge operation [60, 61].

The temporal evolution of the discharge current composition at the target surface is shown in figure 7 for various discharge voltages. We see that the initial peak in the discharge current that was noted in figure 2 is due to Ar^+ ions, which dominate in the beginning of the pulse. For all cases the W^+ ions take over as dominating charged heavy species, as the initial Ar^+ peak decays. This is more pronounced for the higher discharge voltages as the contribution of the W^+ ions to the total discharge current at the target surface increases with increased discharge voltage. Therefore, in the beginning of the pulse the working gas ions bombard the target and sputter off metal atoms that are ionized and consequently return to the target, and constitute a SS recycling loop [23]. Consequently, tungsten atoms and ions, partially take over the role of the working gas argon atoms and ions as the pulse progresses. For a tungsten target Anders *et al* [62] observed an initial peak in the discharge current waveform and argued that the initial peak increases with increased argon pressure, whereas the level of the discharge current plateau later in the pulse is practically independent on the working gas pressure. Therefore, for the initial part of the pulse, working gas sputtering dominates, while the plateau is driven by self-sputtering. For a discharge voltage of 700 V or higher the W^+ ion contribution

Figure 4. The temporal evolution of the neutral particle densities for discharge voltages of (a) 500 V, (b) 600 V, (c) 700 V, and (d) 800 V, for a discharge with 75 mm diameter tungsten target.
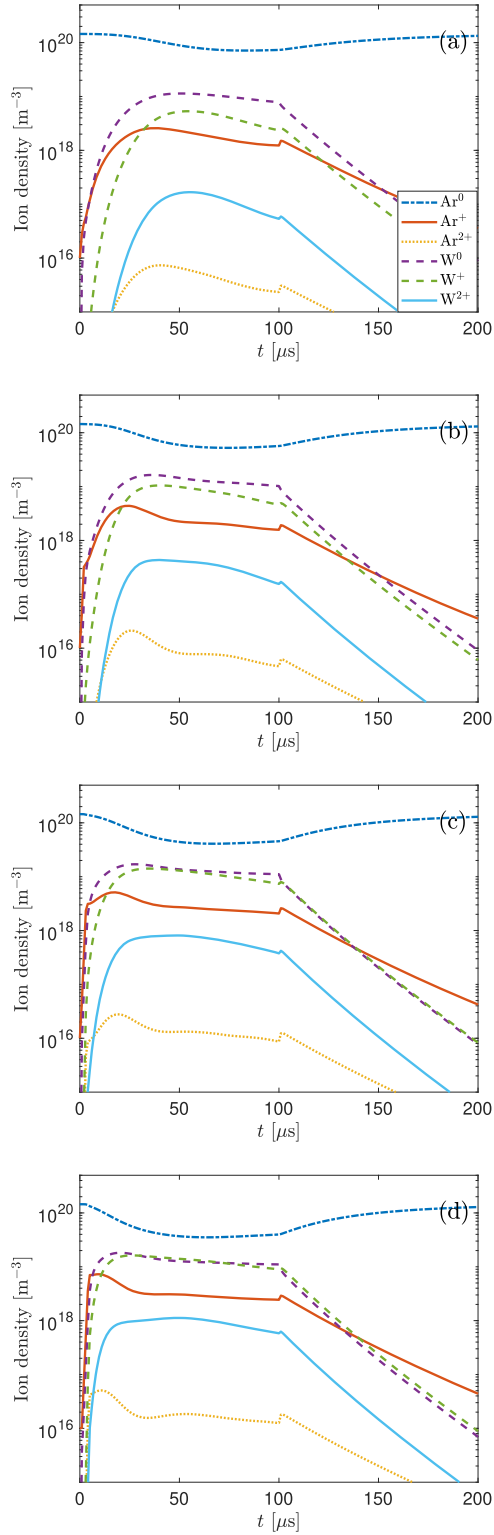
rapidly at the beginning of the pulse and peaks at 4 μs into the 100 μs long pulse. The emission from the Ar^+ ions peaks a few microseconds into the pulse and then decays. This is followed by an increase in emission from atomic W and W^+ ions which indicates ejection of tungsten atoms from the target and subsequent ionization. The emission from the W^+ ions peaks
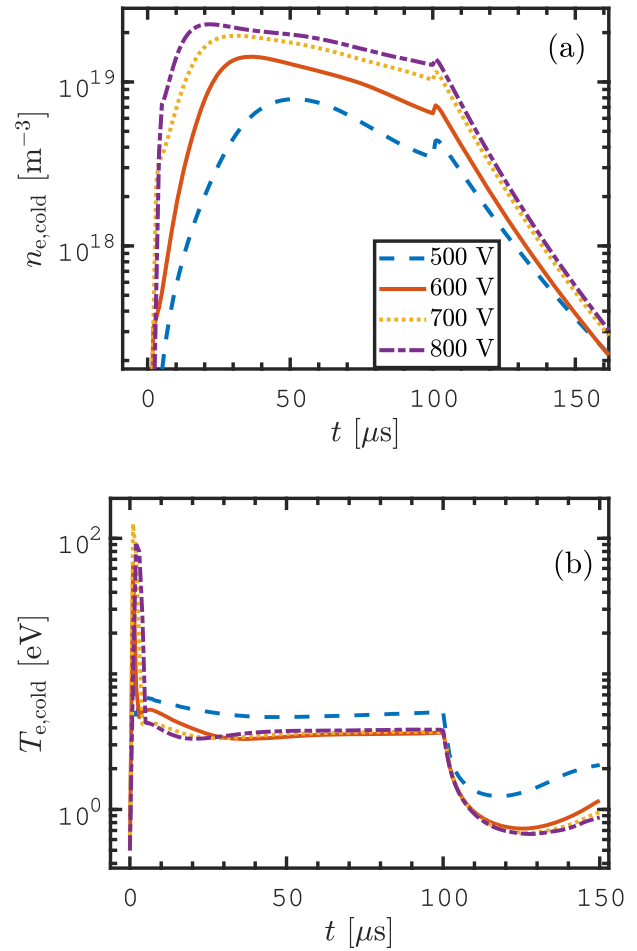
Figure 6. The temporal evolution of the charged particle densities for discharge voltages of (a) 500 V, (b) 600 V, (c) 700 V, and (d) 800 V, for a discharge with 75 mm diameter tungsten target. In addition we also show the total argon neutral density (ground state and excited states) [Ar^0] and the neutral tungsten density [W^0].
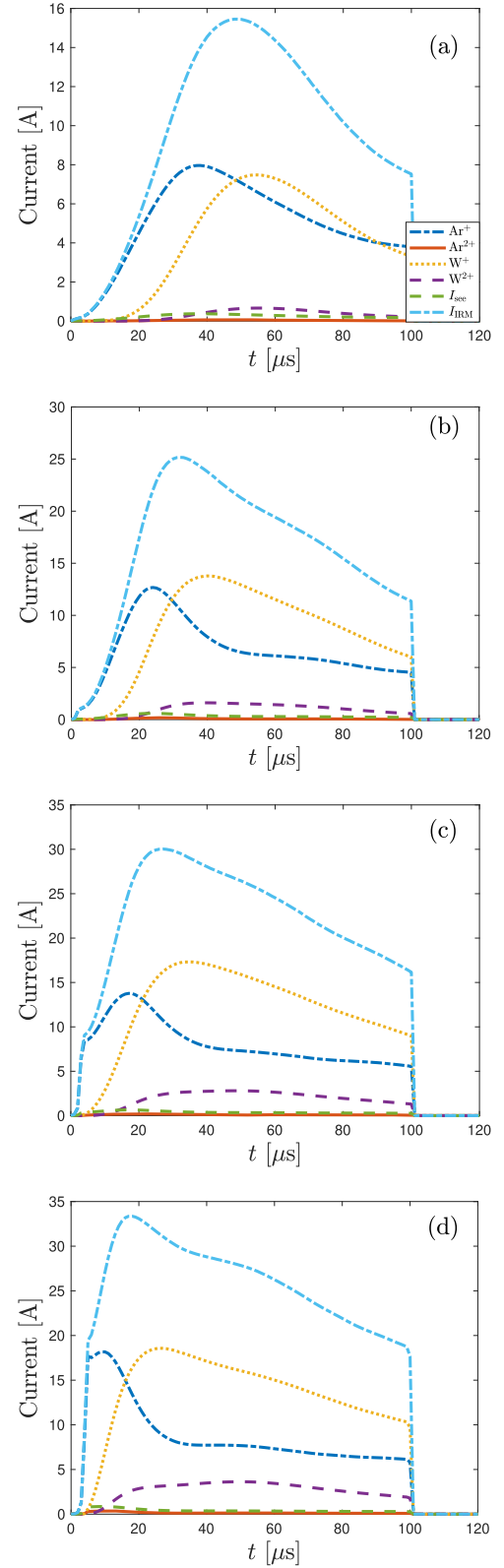
Figure 7. The temporal evolution of the discharge current composition at the target surface for discharge voltages of (a) 500 V, (b) 600 V, (c) 700 V, and (d) 800 V, for a discharge with 75 mm diameter tungsten target.

to the discharge current is much higher than the Ar$^+$ ion contribution. Our findings agree with the earlier work of Anders *et al* [62] who see an initial peak when the discharge voltage was 700 V or higher. They pointed out that the initial peak increases steeply indicating that the argon working gas is very efficiently ionized. There is some, but much smaller contribution, from W^{2+} ions to the discharge current while the contribution of Ar^{2+} ions and secondary electrons are negligible.

The temporal evolution of the electron density is shown in figure 8(a) and the temporal evolution of the electron temperature for the cold electron group is shown in figure 8(b). There is a peak in the electron density early in the pulse. It increases in value and peaks earlier in the pulse with increased discharge voltage. In the electron temperature, we observe a similar a sharp peak early in the pulse for all discharges. The electron temperature reaches a plateau in the range 3.59–5.03 eV as the pulse progresses. Similar spikes in the electron temperature in the beginning of the pulse were observed when modeling a discharge with a copper target operated with argon as working gas at 0.4 and 0.5 Pa [25]. It should also be noted that Pajdarová *et al* [63] experimentally observed a fast rise to high electron temperatures in the initial stages of the pulse, which is followed by a decrease to ∼1 eV, when operating a HiPIMS discharge with Cu target at 1 Pa, and measured outside the IR. Similarly, Poolcharuansin and Bradley [64] reported on three distinct groups of electrons which they referred to as 'super-thermal', 'hot' and 'cold' populations in the initial phase of the voltage pulse (1–4 μs) when operating with a titanium target. High electron temperatures in the beginning of a pulse observed in pulsed inductively coupled discharges were explained by fewer electrons available in the initial stages of the pulse [65, 66]. Therefore, in the initial stages of the pulse all the input power is absorbed by a limited number of electrons and it shows up as a spike in the electron temperature. The electron density and electron temperature have been determined experimentally for both dcMS [67] and HiPIMS [68] discharges with a tungsten target, using Langmuir probe and Thomson scattering. The electron density at the magnetic null point was found to peak at 5×10^{18} m^{-3} in a HiPIMS discharge at 50 μs into a 100 μs long pulse at working gas pressure of 1.6 Pa and peak discharge current density of 0.74 A cm^{-2}. At this time a local minimum in the electron temperature is observed which indicates cooling of the EEDF as the density of metallic species in the discharge increases. As the electrons cool down, the ion generation rate decreases and consequently the sputter rate is reduced. Consequently, the electron temperature rises again, decreasing the electron density [68]. It has been argued that for metals with high sputter yield, such as aluminum and copper, the HiPIMS discharge can be operated in the sustained SS mode and the discharge current is stabilized via a negative feedback mechanism [69]. Increased discharge current leads to increased sputtering, increased presence of metal atoms, and a lower effective electron temperature and, therefore, lower ionization. Furthermore, by comparing various target materials it has been suggested that the ionization fraction of the sputtered species is lower for materials with higher sputter yield as the electron


Figure 8. The temporal evolution of the (a) cold electron density and the (b) cold electron temperature for the various discharge voltages for a discharge with 75 mm diameter tungsten target.

temperature decreases due to increased number of sputtered species [69].

5. Discussion

The model results describe a discharge where the Ar$^+$ ions dominate in the beginning of the pulse and then few tens of μs into the pulse W$^+$ ions take over as the dominating ions as seen in figures 6 and 7. Here we explore how the internal discharge parameters vary with discharge voltage and resulting discharge current. Figure 9 shows the internal discharge parameters, the ionization probability α_t, the back-attraction probability during the pulse $\beta_{t,pulse}$, the overall back-attraction probability β_t, and the fractional potential drop over the IR $f = V_{IR}/V_D$ as a function of the discharge voltage. In figure 9(a) we see that the ionization probability α_t increases while the back-attraction probability $\beta_{t,pulse}$ decreases with increased discharge voltage. Earlier we have argued that the ionization probability depends only on the peak discharge current and increases with increased peak discharge current [70] and the decreasing back-attraction probability with increasing peak discharge current confirms the suggestion made by Brenning *et al* [71, 72]. Recall that the peak discharge current increases with increased discharge voltage (see figure 2), and the peak current density
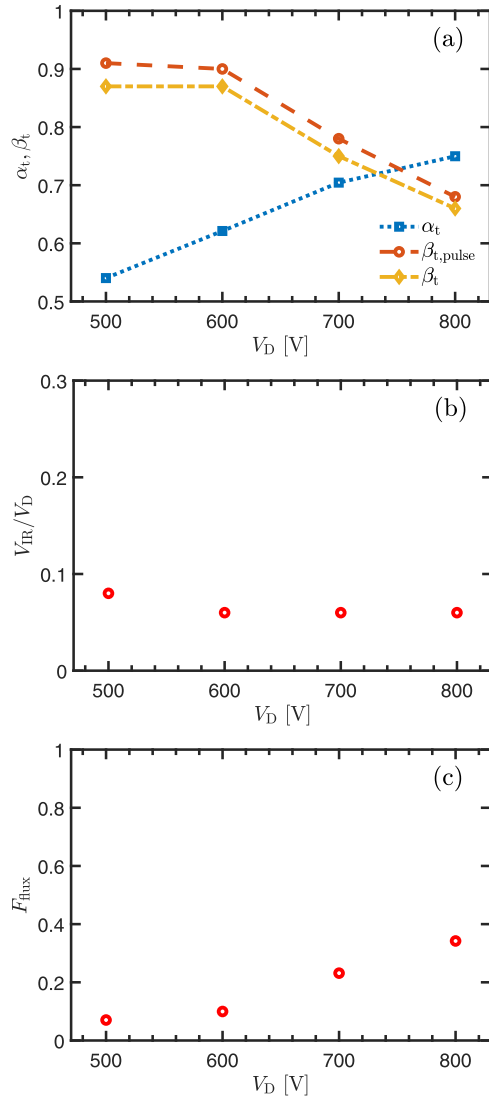
Figure 9. The (a) ionization probability α_t and the back-attraction probability $\beta_{t,pulse}$ and β_t, (b) the fractional potential drop over the IR $f = V_{IR}/V_D$, and (c) the ionized flux fraction versus the discharge voltage V_D determined by the IRM for a discharge with 75 mm diameter tungsten target.

$J_{D,peak}$ in this study is in the range 0.33–0.73 A cm^{-2}. The decrease of $\beta_{t,pulse}$ and β_t with increasing $J_{D,peak}$ can be understood when considering the ideal case of gas-less sputtering, in which there is no working gas. We consider a time span in a steady state discharge during which a number N_{W+} of W$^+$ ions hit the target. They sputter out a number $N_{W+}Y_{SS}$ tungsten atoms. The fraction α_t of the sputtered atoms will become ionized within the IR, and a fraction β_t of the ions will become back-attracted and hit the target. Each chain of events beginning with a W$^+$ ion hitting the target therefore ends with $\alpha_t\beta_tY_{SS}$ target ions hitting the target. In steady state these two numbers of ions are identical and

$$N_{W+} = N_{W+}\alpha_t\beta_tY_{SS} \tag{4}$$

giving

$$\beta_t = \frac{1}{\alpha_tY_{SS}}. \tag{5}$$

As the ionization probability α_t increases with increased discharge current, and the SS yield Y_{SS} increases also slightly (from 0.8 to 1.1), the back-attraction probability has to decrease.

Figure 9(b) shows the fraction of the discharge voltage that drops over the IR versus the discharge voltage. It is 8% at 500 V and 6% at higher discharge voltage. Figure 9(c) shows that the ionized flux fraction F_{flux} increases from 7% for peak current density of 0.33 A cm^{-2} to 34% at 0.73 A cm^{-2}. For comparison, when operating a HiPIMS discharge with a copper target and peak current density $J_{D,peak} \sim 1$ A cm^{-2}, the ionized flux fraction is in the range 32%–40% [25], while when using a titanium target the ionized flux fraction is roughly 30% for $J_{D,peak} \sim 1$ A cm^{-2} and 14%–20% for $J_{D,peak} \sim 0.5$ A cm^{-2} [73].

The generalized recycling model combines the processes of SS-recycling and working gas recycling in HiPIMS discharges [23, 74] and can be used to explain the large discharge currents observed in HiPIMS. In the generalized recycling model it is assumed that a primary current acts as a seed that is amplified by both the SS recycling process and the working gas recycling process. A primary current I_{prim} is defined as a current, which is composed almost entirely of the ions of the working gas, here Ar$^+$ ions, that have been ionized for the first time and then drawn to the target (and maybe a very small contribution from secondary electrons, which we neglect) [24, 74]. This is the dominating current in dcMS discharge operation. However, there is a maximum steady state supply rate of argon atoms from the surrounding gas reservoir [19]. This current therefore has a critical upper limit that can be estimated using

$$I_{crit} = S_{RT}ep_g\sqrt{\frac{1}{2\pi m_gk_BT_g}} = S_{RT}en_g\sqrt{\frac{k_BT_g}{2\pi m_g}}, \tag{6}$$

where p_g is the working gas pressure, T_g is the working gas temperature, n_g is the working gas density and S_{RT} is the racetrack area. For a gas temperature of 300 K, this gives an estimate of the maximum available discharge current due to working gas ions that are ionized for the first time and drawn to the target given in practical units as

$$I_{crit} \approx 0.38p_gS_{RT}, \tag{7}$$

where S_{RT} is the racetrack area in cm^2, and p_g is the working gas pressure in Pa and here we assume $S_{RT} = 0.5 \times S_T$.

For our discharge conditions here, $I_{crit} = 8.4$ A. For discharge currents I_D larger than I_{crit} there has to be some kind of recycling of atoms that leave the target, subsequently become ionized and then are drawn back to the target [23]. This can be either SS recycling or working gas-recycling. For all the cases explored here the discharge current goes well above the critical current during the pulse. The lowest peak discharge current is $I_{D,peak} = 14.6$ A at 500 V and the discharge current increases with increased discharge voltage (see figure 2), and a bigger fraction of the discharge current is due to recycling.
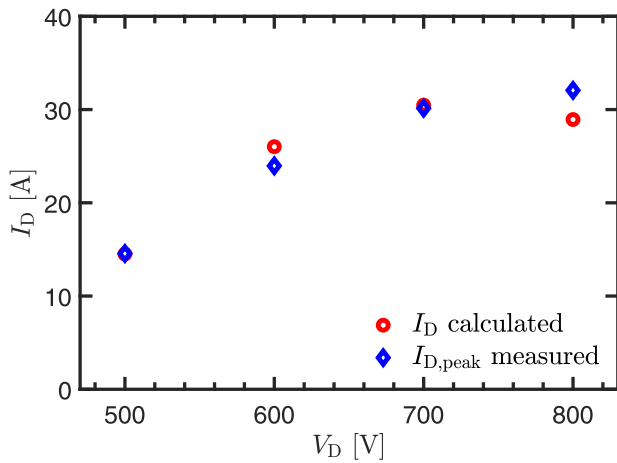
Figure 10. The measured peak discharge current and the discharge current calculated using the internal discharge parameters determined by IRM and equation (9), versus the discharge voltage V_D for a discharge with 75 mm diameter tungsten target.

Earlier we have shown that the discharge current in a HiPIMS discharge is the sum of the primary current, and contributions from working gas recycling and SS recycling, which can be written [23]

$$I_D \approx I_{prim} + I_{gas-recycle} + I_{SS}. \tag{8}$$

The discharge current can also be written as multiplication of the primary current I_{prim} that then acts as a seed [23], which in steady states gives

$$I_D \approx I_{prim} \left(1 + \frac{\pi_g}{1 - \pi_g}\right) \left(1 + \frac{Y_g}{Y_{SS}} \frac{\pi_{SS}}{1 - \pi_{SS}}\right), \tag{9}$$

where the working gas-sputtering parameter is $\pi_g = \alpha_g \beta_{g,pulse} \xi_{pulse}$ and the SS parameter is $\pi_{SS} = \alpha_t \beta_{t,pulse} Y_{SS}$ Here, $\xi_{pulse} = 1$ is the fraction of the recombined Ar^+ ions at the target that is assumed to return during the pulse as a hot argon atom Ar^H or warm argon atom Ar^W.

Figure 10 shows the measured peak discharge current and the discharge current calculated using equation (9) from the internal discharge parameters, that were determined by the IRM (and listed in table 3), versus the discharge voltage V_D. We see that the discharge current determined from the internal discharge parameters using the generalized recycling model agrees well with the measured peak discharge current.

The above discussion and in particular equation (9) is derived assuming that the primary current is at its critical upper limit, and that each subsequent cycle adds another contribution to the working gas and SS recycling current and, assuming a large number of such recycling loops, use the infinite sum $\sum_{n=1}^{\infty} a^n = a/(1 - a)$ where $0 < a < 1$.

To verify the validity of this assumption we estimate the ion loss time based on average quantities. The complete sequence of events to reach equilibrium involves developing both a working gas recycling loop and a target species recycling loop. They come in a sequence of two loops. The working gas recycling loop initiates with an event of argon ionization and involves three steps (i) Ar^+ ion acceleration to the target (i.e., back-attraction), (ii) return to the IR either as a hot or a warm argon atom, and (iii) ionization. Similarly, the SS recycling loop starts with an event of tungsten ionization followed by (i) W^+ ion acceleration to the target, (ii) sputtering that creates a tungsten atom that enters the IR, and (iii) ionization of this atom. To estimate the time of step (i) we assume the average ion that ends up at the target was produced in the middle of the IR, at a distance $(z_2 - z_1)/2$ from the sheath edge, and that the potential difference from this position to the sheath edge is $V_{IR}/2$. The loss time in the IR for this average ion is under these assumptions [19]

$$t_{loss} = \frac{z_2 - z_1}{\sqrt{\frac{q_i V_{IR}}{m_i}}} \tag{10}$$

which for for Ar^+ ion is $t_{loss} \sim 2\ \mu s$ and for W^+ ions the loss time is $t_{loss} \sim 4\ \mu s$, using z_1 and z_2 assumed in the IRM. A different estimate is based on lateral imaging of a HiPIMS discharge by Anders *et al* [75]. They assume the atoms to only travel about 1–3 mm away from the target surface before they are ionized [76]. This leads to estimates for the residence time for Nb^+ ions in the range 0.2–0.3 μs. Scaling this with the square root of the ion mass ratio yields 0.3–0.4 μs for W^+ ions. For steps (ii) and (iii) we separate the time into a transit time t_{trans} and an ionization time t_{ion}. The transit time is the extent of the IR divided by the typical speed in the z-direction. It is longer for warm than for hot Ar atoms. Here we use the notation $\langle t_{trans} \rangle$ for a suitable average. The transit time $\langle t_{trans} \rangle$ is roughly 7.5 μs and 40 μs for hot and warm argon atoms, respectively, and about 13 μs for sputtered tungsten with energy of 4.45 eV. The ionization time for an atom is $t_{ion} = 1/(n_e \times k_{ioniz})$. The ionization time is about 1.5 ms for argon and about 30 μs for tungsten. A returning argon atom from the target can either be ionized in transit through the IR, or pass through it and escape to the DR and therefore the effective time for steps (ii) and (iii) can be approximated as the shorter of these: the time from target to ionization $t_{t,iz} = \min(\langle t_{trans} \rangle, t_{ion})$. The slower of the loops, the SS recycling loop, takes under 17 μs to complete. Therefore, the use of equation (9) is justified.

The ratio of the flux of sputtered species (ions and neutrals) that leave the IR towards the DR Γ_{DR} and the total flux (atoms s^{-1}) of atoms sputtered from the target Γ_0, the useful fraction of the sputtered species, or the normalized deposition rate, can be approximated by [77, 78]

$$F_{dep} = \frac{\Gamma_{DR}}{\Gamma_0} = 1 - \alpha_t \beta_t. \tag{11}$$

This parameter is plotted versus the discharge voltage V_D in figure 11, where it is compared to the measured normalized deposition rate. The measured normalized deposition rate is the deposition rate for HiPIMS operation divided by the deposition rate determined from dcMS operated at the same average power. We see that the normalized deposition rate calculated using the internal discharge parameters determined by the IRM agree well with the measured values. Keep in
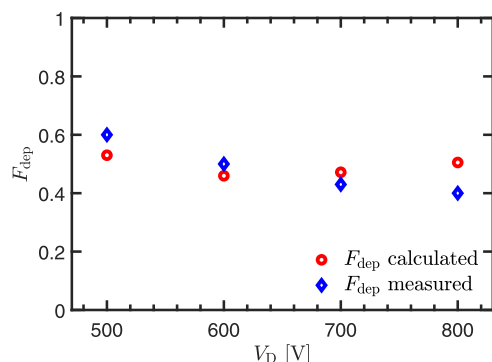
Figure 11. The measured normalized deposition rate and the normalized deposition rate determined from the IRM versus the discharge voltage V_D for a discharge with 75 mm diameter tungsten target.

mind that equation (11) does not take into account ion focusing (or spreading) en route towards the substrate [53, 73]. Equation (11) says that this normalized deposition rate is reduced, and the fraction of the sputtered species reaching the substrate decreases, as the ionization of the sputtered material increases.

6. Conclusions

We have explored the effect of the discharge voltage on the plasma parameters, including the internal discharge parameters, of a HiPIMS discharge in argon with tungsten target operated in the current density range 0.33–0.73 A cm^{-2}. The temporal evolution of the densities of the various species that constitute the discharge is reported and evaluated along with various plasma parameters. Ar$^+$ ions dominate the discharge current at the target surface in the beginning of the pulse, while later in the pulse W$^+$ ions dominate the discharge current for the remainder of the pulse duration. The ionization probability of tungsten increases, while the back-attraction probability decreases, with increased discharge voltage. The gas rarefaction toward the end of the pulse reaches values in the range 57%–76%. The findings, on the ionization probability and the back-attraction probability, were used as an input into the generalized recycling model to estimate the peak discharge current. The results are in good agreement with experimental values. Furthermore, the measured normalized deposition rate is compared to values determined from the internal discharge parameters from the IRM, with good agreement.

Acknowledgments

Data availability statement

The data that support the findings of this study are available upon reasonable request from the authors.

ORCID iDs

Swetha Suresh Babu [ID] https://orcid.org/0000-0001-5360-5562
Martin Rudolph [ID] https://orcid.org/0000-0002-0854-6708
Daniel Lundin [ID] https://orcid.org/0000-0001-8591-1003
Tetsuhide Shimizu [ID] https://orcid.org/0000-0002-7810-3777
Joel Fischer [ID] https://orcid.org/0000-0001-9116-6302
Michael A Raadu [ID] https://orcid.org/0000-0002-1299-5039
Nils Brenning [ID] https://orcid.org/0000-0003-1308-9270
Jon Tomas Gudmundsson [ID] https://orcid.org/0000-0002-8153-3209

References

[1] Waits R K 1978 *J. Vac. Sci. Technol.* **15** 179
[2] Gudmundsson J T 2020 *Plasma Sources Sci. Technol.* **29** 113001
[3] Krüger D, Köhn K, Gallian S and Brinkmann R P 2018 *Phys. Plasmas* **25** 061207
[4] Gudmundsson J T and Lundin D 2020 *High Power Impulse Magnetron Sputtering: Fundamentals, Technologies, Challenges and Applications* ed D ed Lundin, T Minea and J T Gudmundsson (Amsterdam: Elsevier) pp 1–48
[5] Helmersson U, Lattemann M, Bohlmark J, Ehiasarian A P and Gudmundsson J T 2006 *Thin Solid Films* **513** 1
[6] Greczynski G, Petrov I, Greene J E and Hultman L 2019 *J. Vac. Sci. Technol.* A **37** 060801
[7] Rossnagel S M, Noyan I C and Cabral C 2002 *J. Vac. Sci. Technol.* B **20** 2047
[8] Choi D *et al* 2011 *J. Vac. Sci. Technol.* A **29** 051512
[9] Naujoks D *et al* 1996 *Nucl. Fusion* **36** 671
[10] Pitts R A *et al* 2013 *J. Nucl. Mater.* **438** S48
[11] Najafi-Ashtiani H, Akhavan B, Jing F and Bilek M M 2019 *ACS Appl. Mater. Interfaces* **11** 14871
[12] Haviar S, Čapek J, Batková Š, Kumar N, Dvořák F, Duchoň T, Fialová M and Zeman P 2018 *Int. J. Hydrog. Energy* **43** 22756
[13] Engwall A M, Shin S J, Bae J and Wang Y M 2019 *Surf. Coat. Technol.* **363** 191
[14] Roychowdhury T, Shah D, Jain V, Patel D I, Dodson B, Skinner W, Hilfiker J N, Smith S J and Linford M R 2020 *Surf. Interface Anal.* **52** 433
[15] Shimizu T, Takahashi K, Boyd R, Viloan R P, Keraudy J, Lundin D, Yang M and Helmersson U 2021 *J. Appl. Phys.* **129** 155305
[16] Velicu I-L, Tiron V, Porosnicu C, Burducea I, Lupu N, Stoian G, Popa G and Munteanu D 2017 *Appl. Surf. Sci.* **424** 397
[17] Velicu I-L, Tiron V, Mihaila I and Costin C 2018 Pulsed magnetron sputtering: the role of the applied power on W coatings properties *Recent Advances in Technology Research and Education Advances in Intelligent Systems and Computing* vol 660 ed D Luca, L Sirghi and C Costin (Berlin: Springer) pp 183–90
[18] Raadu M A, Axnäs I, Gudmundsson J T, Huo C and Brenning N 2011 *Plasma Sources Sci. Technol.* **20** 065007
[19] Huo C, Lundin D, Gudmundsson J T, Raadu M A, Bradley J W and Brenning N 2017 *J. Phys. D: Appl. Phys.* **50** 354003
[20] Rudolph M, Brenning N, Raadu M A, Hajihoseini H, Gudmundsson J T, Anders A and Lundin D 2020 *Plasma Sources Sci. Technol.* **29** 05LT01

[21] Huo C, Lundin D, Raadu M A, Anders A, Gudmundsson J T and Brenning N 2013 *Plasma Sources Sci. Technol.* **22** 045005

[22] Eliasson H *et al* 2021 *Plasma Sources Sci. Technol.* **30** 115017

[23] Brenning N, Gudmundsson J T, Raadu M A, Petty T J, Minea T and Lundin D 2017 *Plasma Sources Sci. Technol.* **26** 125003

[24] Huo C, Lundin D, Raadu M A, Anders A, Gudmundsson J T and Brenning N 2014 *Plasma Sources Sci. Technol.* **23** 025017

[25] Gudmundsson J T, Fischer J, Hinriksson B P, Rudolph M and Lundin D 2022 *Surf. Coat. Technol.* **442** 128189

[26] Gudmundsson J T, Lundin D, Brenning N, Raadu M A, Huo C and Minea T M 2016 *Plasma Sources Sci. Technol.* **25** 065004

[27] Lundin D, Gudmundsson J T, Brenning N, Raadu M A and Minea T M 2017 *J. Appl. Phys.* **121** 171917

[28] Rezek J, Kozák T, Kumar N and Haviar S 2021 *J. Phys. D: Appl. Phys.* **54** 125202

[29] Rudolph M, Revel A, Lundin D, Hajihoseini H, Brenning N, Raadu M A, Anders A, Minea T M and Gudmundsson J T 2021 *Plasma Sources Sci. Technol.* **30** 045011

[30] Stancu G D, Brenning N, Vitelaru C, Lundin D and Minea T 2015 *Plasma Sources Sci. Technol.* **24** 045011

[31] Gudmundsson J T, Lundin D, Stancu G D, Brenning N and Minea T M 2015 *Phys. Plasmas* **22** 113508

[32] Gudmundsson J T and Thorsteinsson E G 2007 *Plasma Sources Sci. Technol.* **16** 399

[33] Alves L L 2014 *J. Phys.: Conf. Ser.* **565** 012007

[34] Alves L L and Guerra V 2020 IST-Lisbon database www.lxcat.net/ist-lisbon retrieved on (18 May 2020)

[35] Dixon A J, Harrison M F A and Smith A C H 1973 *8th Int. Conf. Physics of Electronic and Atomic Collisions (VIII ICPEAC)* ed B C ed Cobić and M V Kurepa (Beograd: Institute of Physics) pp 405–6

[36] Freund R S 1987 *Swarm Studies and Inelastic Electron–Molecule Collisions Proc. Meeting of the 4th Int. Swarm Seminar and the Inelastic Electron–Molecule Collisions Symp.* (Tahoe City, California, USA 19–23 July 1985) ed L C Pitchford, B V McKoy, A Chutjian and S Trajrnar (New York: Springer) pp 329–46

[37] Müller A, Salzborn E, Frodl R, Becker R, Klein H and Winter H 1980 *J. Phys. B: At. Mol. Opt. Phys.* **13** 1877

[38] Stephan K, Helm H and Märk T D 1980 *J. Chem. Phys.* **73** 3763

[39] Deutsch H, Hilpert K, Becker K, Probst M and Märk T D 2001 *J. Appl. Phys.* **89** 1915

[40] Montague R G and Harrison M F A 1984 *J. Phys. B: At. Mol. Opt. Phys.* **17** 2707

[41] Rae S C and Tobin R C 1988 *J. Appl. Phys.* **64** 1418

[42] Anders A 2010 *J. Vac. Sci. Technol.* A **28** 783

[43] Biersack J P and Haggmark L G 1980 *Nucl. Instrum. Methods* **174** 257

[44] Kittel C 2005 *Introduction to Solid State Physics* 8th edn (New York: Wiley)

[45] Riseberg L A, Parks W F and Schearer L D 1973 *Phys. Rev.* A **8** 1962

[46] Inaba S, Goto T and Hattori S 1983 *J. Phys. Soc. Japan* **52** 1164

[47] Bogaerts A, Gijbels R and Carman R J 1998 *Spectrochim. Acta* B **53** 1679

[48] Hotop H and Niehaus A 1969 *Z. Phys.* A **228** 68

[49] Lieberman M A and Lichtenberg A J 2005 *Principles of Plasma Discharges and Materials Processing* 2nd edn (New York: Wiley)

[50] Blanco F, da Silva F F, Limão-Vieira P and García G 2017 *Plasma Sources Sci. Technol.* **26** 085004

[51] Hagstrum H D 1956 *Phys. Rev.* **104** 317

[52] Huo C, Raadu M A, Lundin D, Gudmundsson J T, Anders A and Brenning N 2012 *Plasma Sources Sci. Technol.* **21** 045004

[53] Butler A, Brenning N, Raadu M A, Gudmundsson J T, Minea T and Lundin D 2018 *Plasma Sources Sci. Technol.* **27** 105005

[54] Thornton J A 1978 *J. Vac. Sci. Technol.* **15** 171

[55] Brenning N, Huo C, Lundin D, Raadu M A, Vitelaru C, Stancu G D, Minea T and Helmersson U 2012 *Plasma Sources Sci. Technol.* **21** 025005

[56] Rossnagel S M 1988 *J. Vac. Sci. Technol.* A **6** 19

[57] Alami J, Sarakinos K, Mark G and Wuttig M 2006 *Appl. Phys. Lett.* **89** 154104

[58] Vlček J, Pajdarová A D and Musil J 2004 *Contrib. Plasma Phys.* **44** 426

[59] Vitelaru C, Lundin D, Stancu G D, Brenning N, Bretagne J and Minea T 2012 *Plasma Sources Sci. Technol.* **21** 025010

[60] Bohlmark J, Lattemann M, Gudmundsson J T, Ehiasarian A P, Aranda Gonzalvo Y, Brenning N and Helmersson U 2006 *Thin Solid Films* **515** 1522

[61] Greczynski G and Hultman L 2010 *Vacuum* **84** 1159

[62] Anders A, Andersson J and Ehiasarian A 2007 *J. Appl. Phys.* **102** 113303

[63] Pajdarová A D, Vlček J, Kudláček P and Lukáš J 2009 *Plasma Sources Sci. Technol.* **18** 025008

[64] Poolcharuansin P and Bradley J W 2010 *Plasma Sources Sci. Technol.* **19** 025010

[65] Ashida S, Lee C and Lieberman M A 1995 *J. Vac. Sci. Technol.* A **13** 2498

[66] Ashida S, Shim M R and Lieberman M A 1996 *J. Vac. Sci. Technol.* A **14** 391

[67] Ryan P J, Bradley J W and Bowden M D 2019 *Phys. Plasmas* **26** 073515

[68] Ryan P J, Bradley J W and Bowden M D 2019 *Phys. Plasmas* **26** 040702

[69] Zheng B *et al* 2019 *IEEE Trans. Plasma Sci.* **47** 193

[70] Rudolph M, Brenning N, Hajihoseini H, Raadu M A, Minea T M, Anders A, Gudmundsson J T and Lundin D 2022 *J. Phys. D: Appl. Phys.* **55** 015202

[71] Brenning N, Butler A, Hajihoseini H, Rudolph M, Raadu M A, Gudmundsson J T, Minea T and Lundin D 2020 *J. Vac. Sci. Technol.* A **38** 033008

[72] Brenning N, Hajihoseini H, Rudolph M, Raadu M A, Gudmundsson J T, Minea T M and Lundin D 2021 *Plasma Sources Sci. Technol.* **30** 015015

[73] Rudolph M, Hajihoseini H, Raadu M A, Gudmundsson J T, Brenning N, Minea T M, Anders A and Lundin D 2021 *J. Appl. Phys.* **129** 033303

[74] Anders A, Čapek J, Hála M and Martinu L 2012 *J. Phys. D: Appl. Phys.* **45** 012003

[75] Anders A, Ni P and Rauch A 2012 *J. Appl. Phys.* **111** 053304

[76] Anders A 2012 *Appl. Phys. Lett.* **100** 224104

[77] Bradley J W, Mishra A and Kelly P J 2015 *J. Phys. D: Appl. Phys.* **48** 215202

[78] Hajihoseini H, Čada M, Hubička Z, Ünaldi S, Raadu M A, Brenning N, Gudmundsson J T and Lundin D 2019 *Plasma* **2** 201